



**AFRL-RX-WP-JA-2014-0178**

**EFFECT OF ALUMINUM ON THE MICROSTRUCTURE  
AND PROPERTIES OF TWO REFRACTORY HIGH-  
ENTROPY ALLOYS (POSTPRINT)**

**O.N. Senkov , S.V. Senkova, and C. Woodward  
AFRL/RXCM**

**APRIL 2014  
Interim Report**

**Distribution A. Approved for public release; distribution unlimited.**

*See additional restrictions described on inside pages*

**STINFO COPY**

**© 2014 Acta Materialia Inc.**

**AIR FORCE RESEARCH LABORATORY  
MATERIALS AND MANUFACTURING DIRECTORATE  
WRIGHT-PATTERSON AIR FORCE BASE, OH 45433-7750  
AIR FORCE MATERIEL COMMAND  
UNITED STATES AIR FORCE**

## NOTICE AND SIGNATURE PAGE

Using Government drawings, specifications, or other data included in this document for any purpose other than Government procurement does not in any way obligate the U.S. Government. The fact that the Government formulated or supplied the drawings, specifications, or other data does not license the holder or any other person or corporation; or convey any rights or permission to manufacture, use, or sell any patented invention that may relate to them.

This report was cleared for public release by the USAF 88th Air Base Wing (88 ABW) Public Affairs Office (PAO) and is available to the general public, including foreign nationals.

Copies may be obtained from the Defense Technical Information Center (DTIC)  
(<http://www.dtic.mil>).

AFRL-RX-WP-JA-2014-0178 HAS BEEN REVIEWED AND IS APPROVED FOR  
PUBLICATION IN ACCORDANCE WITH ASSIGNED DISTRIBUTION STATEMENT.

//Signature//

---

CHRISTOPHER F. WOODWARD  
Metals Branch  
Structural Materials Division

//Signature//

---

DANIEL J. EVANS, Chief  
Metals Branch  
Structural Materials Division

//Signature//

---

TIMOTHY J. SCHUMACHER, Chief  
Structural Materials Division  
Materials and Manufacturing Directorate

This report is published in the interest of scientific and technical information exchange, and its publication does not constitute the Government's approval or disapproval of its ideas or findings.

REPORT DOCUMENTATION PAGE			Form Approved OMB No. 074-0188	
Public reporting burden for this collection of information is estimated to average 1 hour per response, including the time for reviewing instructions, searching existing data sources, gathering and maintaining the data needed, and completing and reviewing this collection of information. Send comments regarding this burden estimate or any other aspect of this collection of information, including suggestions for reducing this burden to Defense, Washington Headquarters Services, Directorate for Information Operations and Reports, 1215 Jefferson Davis Highway, Suite 1204, Arlington, VA 22202-4302. Respondents should be aware that notwithstanding any other provision of law, no person shall be subject to any penalty for failing to comply with a collection of information if it does not display a currently valid OMB control number. PLEASE DO NOT RETURN YOUR FORM TO THE ABOVE ADDRESS.				
1. REPORT DATE (DD-MM-YYYY) April 2014		2. REPORT TYPE Interim		3. DATES COVERED (From – To) 19 March 2014 – 31 March 2014
4. TITLE AND SUBTITLE EFFECT OF ALUMINUM ON THE MICROSTRUCTURE AND PROPERTIES OF TWO REFRACTORY HIGH-ENTROPY ALLOYS (POSTPRINT)		5a. CONTRACT NUMBER In-House		
		5b. GRANT NUMBER		
		5c. PROGRAM ELEMENT NUMBER 62102F		
6. AUTHOR(S) O.N. Senkov , S.V. Senkova, and C. Woodward		5d. PROJECT NUMBER 4349		
		5e. TASK NUMBER		
		5f. WORK UNIT NUMBER X0W6		
7. PERFORMING ORGANIZATION NAME(S) AND ADDRESS(ES) AFRL/RXCM Air Force Research Laboratory Materials and Manufacturing Directorate Wright-Patterson Air Force Base, OH 45433-7750		8. PERFORMING ORGANIZATION REPORT NUMBER		
9. SPONSORING / MONITORING AGENCY NAME(S) AND ADDRESS(ES) Air Force Research Laboratory Materials and Manufacturing Directorate Wright Patterson Air Force Base, OH 45433-7750 Air Force Materiel Command United States Air Force		10. SPONSOR/MONITOR'S ACRONYM(S)  AFRL/RXCM		
		11. SPONSOR/MONITOR'S REPORT NUMBER(S) AFRL-RX-WP-JA-2014-0178		
12. DISTRIBUTION / AVAILABILITY STATEMENT Distribution A. Approved for public release; distribution unlimited. This report contains color.				
13. SUPPLEMENTARY NOTES PA Case Number: 88ABW-2014-2746; Clearance Date: 5 June 2014. Journal article published in Acta Materialia 68 (2014) 214-228. The U.S. Government is joint author of the work and has the right to use, modify, reproduce, release, perform, display or disclose the work. The final publication is available at <a href="http://dx.doi.org/10.1016/j.actamat.2014.01.029">http://dx.doi.org/10.1016/j.actamat.2014.01.029</a> . See also AFRL-RX-WP-TP-2014-0134, AFRL-RX-WP-JA-2014-0167, AFRL-RX-WP-JA-2014-0170, and AFRL-RX-WP-JA-2014-0177.				
14. ABSTRACT The microstructure, phase composition and mechanical properties of the $\text{AlMo}_{0.5}\text{NbTa}_{0.5}\text{TiZr}$ and $\text{Al}_{0.4}\text{Hf}_{0.6}\text{NbTaTiZr}$ high-entropy alloys are reported. The $\text{AlMo}_{0.5}\text{NbTa}_{0.5}\text{TiZr}$ alloy consists of two body-centered cubic (bcc) phases with very close lattice parameters, $\alpha_1 = 326.8$ pm and $\alpha_2 = 332.4$ pm. One phase was enriched with Mo, Nb and Ta and another phase was enriched with Al and Zr. The phases formed nano-lamellae modulated structure inside equiaxed grains. The alloy had a density of $\rho = 7.40$ g cm <sup>-3</sup> and Vickers hardness $H_v = 5.8$ GPa. Its yield strength was 2000 MPa at 298 K and 745 MPa at 1273 K. The $\text{Al}_{0.4}\text{Hf}_{0.6}\text{NbTaTiZr}$ had a single-phase bcc structure, with the lattice parameter $\alpha = 336.7$ pm. This alloy had a density $\rho = 9.05$ g cm <sup>-3</sup> , Vickers microhardness $H_v = 4.9$ GPa, and its yield strength at 298 K and 1273 K was 1841 MPa and 298 MPa, respectively. The properties of these Al-containing alloys were compared with the properties of the parent $\text{CrMo}_{0.5}\text{NbTa}_{0.5}\text{TiZr}$ and $\text{HfNbTaTiZr}$ alloys and the beneficial effects from the Al additions on the microstructure and properties were outlined. A thermodynamic calculation of the solidification and equilibrium phase diagrams was conducted for these alloys and the calculated results were compared with the experimental data.				
15. SUBJECT TERMS refractory alloys; phase composition; crystal structure; microstructure; mechanical properties				
16. SECURITY CLASSIFICATION OF:			17. LIMITATION OF ABSTRACT  SAR	18. NUMBER OF PAGES  18
a. REPORT Unclassified	b. ABSTRACT Unclassified	c. THIS PAGE Unclassified		
			19a. NAME OF RESPONSIBLE PERSON (Monitor) Christopher F. Woodward	
			19b. TELEPHONE NUBER (include area code) (937) 255-9816	

# Effect of aluminum on the microstructure and properties of two refractory high-entropy alloys

O.N. Senkov\*, S.V. Senkova, C. Woodward

Air Force Research Laboratory, Materials and Manufacturing Directorate, Wright-Patterson AFB, OH 45433, USA

Received 16 August 2013; received in revised form 5 November 2013; accepted 19 January 2014

Available online 23 February 2014

## Abstract

The microstructure, phase composition and mechanical properties of the  $\text{AlMo}_{0.5}\text{NbTa}_{0.5}\text{TiZr}$  and  $\text{Al}_{0.4}\text{Hf}_{0.6}\text{NbTaTiZr}$  high-entropy alloys are reported. The  $\text{AlMo}_{0.5}\text{NbTa}_{0.5}\text{TiZr}$  alloy consists of two body-centered cubic (bcc) phases with very close lattice parameters,  $a_1 = 326.8$  pm and  $a_2 = 332.4$  pm. One phase was enriched with Mo, Nb and Ta and another phase was enriched with Al and Zr. The phases formed nano-lamellae modulated structure inside equiaxed grains. The alloy had a density of  $\rho = 7.40$  g cm<sup>-3</sup> and Vickers hardness  $H_v = 5.8$  GPa. Its yield strength was 2000 MPa at 298 K and 745 MPa at 1273 K. The  $\text{Al}_{0.4}\text{Hf}_{0.6}\text{NbTaTiZr}$  had a single-phase bcc structure, with the lattice parameter  $a = 336.7$  pm. This alloy had a density  $\rho = 9.05$  g cm<sup>-3</sup>, Vickers microhardness  $H_v = 4.9$  GPa, and its yield strength at 298 K and 1273 K was 1841 MPa and 298 MPa, respectively. The properties of these Al-containing alloys were compared with the properties of the parent  $\text{CrMo}_{0.5}\text{NbTa}_{0.5}\text{TiZr}$  and  $\text{HfNbTaTiZr}$  alloys and the beneficial effects from the Al additions on the microstructure and properties were outlined. A thermodynamic calculation of the solidification and equilibrium phase diagrams was conducted for these alloys and the calculated results were compared with the experimental data.

© 2014 Acta Materialia Inc. Published by Elsevier Ltd. All rights reserved.

**Keywords:** Refractory alloys; Phase composition; Crystal structure; Microstructure; Mechanical properties

## 1. Introduction

Multi-principal-element alloys, also known as high-entropy alloys (HEAs) because of their high entropy of mixing of alloying elements, have recently come to the attention of the scientific community due to some interesting and unexpected microstructures and properties [1–3]. The metallurgical strategy is to stabilize the disordered phase relative to impinging ordered intermetallics by maximizing the configurational entropy. One appealing aspect of this approach is that the reduction of the Gibbs free energy, by the entropy of formation, increases with an increase in temperature. Such an approach could be very useful in developing new high-temperature structural

alloys, in an alloy composition space that has not been previously explored. While the HEA approach has produced some stable solid solution body-centered-cubic (bcc) and face-centered-cubic (fcc) alloys [1,4–9], recent studies have shown that intermetallic phases can form in HEAs. This often is associated with alloying with elements with large differences in atomic radius and large negative enthalpies of mixing [4,10,11].

Several high-entropy refractory alloys with promising combinations of room temperature and elevated temperature mechanical properties and oxidation resistance have recently been reported. These are MoNbTaW, MoNbTaVW [6,7], HfNbTaTiZr [8,9],  $\text{CrMo}_{0.5}\text{NbTa}_{0.5}\text{TiZr}$  [12,13] and  $\text{Cr}_x\text{NbTiV}_y\text{Zr}$  [14,15]. The high entropy of mixing and similar atomic radii (e.g.  $\sim 146$  pm) of the alloying elements resulted in the formation of disordered bcc crystal structures in the alloys without Cr. However, the alloys

\* Corresponding author. Tel.: +1 937 255 4064.

E-mail address: [oleg.senkov@wpafb.af.mil](mailto:oleg.senkov@wpafb.af.mil) (O.N. Senkov).

with Cr, the atomic radius ( $r_{\text{Cr}} = 128$  pm) of which is much smaller than the atomic radii of other elements, additionally contained a cubic Laves phase, resulting in a considerable decrease in ductility at temperatures below 800 °C [12,14,15].

In the present work, the compositions of two earlier reported refractory alloys, HfNbTaTiZr and CrMo<sub>0.5</sub>NbTa<sub>0.5</sub>TiZr, have been modified to produce the Al<sub>0.4</sub>Hf<sub>0.6</sub>NbTaTiZr and AlMo<sub>0.5</sub>NbTa<sub>0.5</sub>TiZr alloys. Here we study the effect of alloying with Al on the microstructure, composition and mechanical properties of these new refractory HEAs. Aluminum forms a number of binary and ternary intermetallic phases with bcc refractory elements. At the same time, the atomic radius of Al ( $r_{\text{Al}} = 143$  pm) is very similar to the atomic radii of the refractory elements ( $\langle r \rangle = 146$  pm), excluding Cr ( $r_{\text{Cr}} = 128$  pm), which may affect the formation energy of the intermetallic phases in the HEAs. Furthermore, it has been well documented that additions of Al stabilize the bcc crystal structure in the Al<sub>x</sub>CoCrCuFeNi [1] and Al<sub>x</sub>CoCrFeMnNi [16] HEAs and gradually transform their crystal structure from fcc to bcc. It is also expected that alloying with Al will considerably reduce the density of the refractory HEAs.

## 2. Experimental procedures

The AlMo<sub>0.5</sub>NbTa<sub>0.5</sub>TiZr and Al<sub>0.4</sub>Hf<sub>0.6</sub>NbTaTiZr HEAs were prepared by vacuum arc melting of nominal mixtures of the corresponding elements. Titanium, zirconium and hafnium were in the form of 3.2 mm diameter slugs with purities of 99.98%, 99.95% and 99.9%, respectively. Niobium and tantalum were in the form of 1.0 and 2.0 mm wires, and their purities were 99.95% and 99.9%, respectively. Molybdenum was in the form of 1 mm thick sheet with a purity of 99.99%. Aluminum was in the form of 50–100 mm<sup>3</sup> buttons with a purity of 99.999%. Arc melting was conducted on a water-cooled copper plate. High-purity molten titanium was used as a getter for residual oxygen, nitrogen and hydrogen. To achieve a homogeneous distribution of elements in the alloys, each alloy was re-melted five times, was flipped for each melt, and was in a liquid state for ~5 min during each melting event. The prepared specimens were ~12 mm high, 30 mm wide and 100 mm long and had shiny surfaces, indicating minimal oxidation during vacuum arc melting. The actual alloy compositions, determined with inductively coupled plasma-optical emission spectroscopy, are given in Table 1. The AlMo<sub>0.5</sub>NbTa<sub>0.5</sub>TiZr alloy was hot isostatically pressed (HIPed) at 1673 K and 207 MPa for 2 h and then annealed at 1673 K for 24 h in continuously flowing

high-purity argon. The Al<sub>0.4</sub>Hf<sub>0.6</sub>NbTaTiZr alloy was HIPed at 1473 K and 207 MPa for 2 h and then annealed at 1473 K for 24 h in continuously flowing high-purity argon. During HIP and annealing, the samples were covered with Ta foil to minimize oxidation. The cooling rate after annealing in both cases was 10 K min<sup>−1</sup>. The crystal structure was identified with the use of an X-ray diffractometer, Cu K $\alpha$  radiation and a  $2\theta$  scattering range of 10–140°. The experimental error in the measurements of the lattice parameters was  $\pm 0.5$  pm.

Alloy densities were measured with an AccuPyc 1330 V1.03 helium pycnometer. Vickers microhardness was measured on polished cross-section surfaces using a 136° Vickers diamond pyramid under 500 g load applied for 20 s. The microstructure was analyzed with a scanning electron microscope (SEM) Quanta 600F (FEI, North America NanoPort, Hillsboro, Oregon, USA) equipped with backscatter electron (BSE), energy-dispersive X-ray spectroscopy (EDS) and electron backscatter diffraction detectors. The experimental error in the measurements of the chemical composition was  $\pm 0.3$  at.%. The average grain/particle size and the volume fractions of the phases were determined in accordance with ASTM E112 and ASTM E562 standards, using the image analysis software Fovea Pro 4.0 by Reindeer Graphics, Inc.

Compression tests of rectangular specimens with the dimensions of  $\sim 4.7$  mm  $\times$  4.7 mm  $\times$  7.7 mm were conducted at 298 K, 873 K, 1073 K, 1273 K and 1473 K in a computer-controlled Instron (Instron, Norwood, MA) mechanical testing machine outfitted with a Brew vacuum furnace and silicon carbide dies. Prior to each test, the furnace chamber was evacuated to  $\sim 10^{-4}$  N m<sup>−2</sup>. The test specimen was then heated to the test temperature at a heating rate of  $\sim 20$  K min<sup>−1</sup>, soaked at the test temperature for 15 min under 5 N controlled load and then compressed to a 50% height reduction or to fracture, whichever happened first. A constant ramp speed that corresponded to an initial strain rate of  $10^{-3}$  s<sup>−1</sup> was used. Room temperature tests were conducted at the same loading conditions but in air. The deformation of all specimens was video-recorded and image correlation software Vic-Gauge (Correlated Solutions, Inc.) was used to measure strains.

## 3. Results

### 3.1. Crystal structure, density and microhardness

X-ray diffraction patterns of the annealed cast alloys are shown in Fig. 1. Two phases, both with the bcc crystal structures, are identified in the AlMo<sub>0.5</sub>NbTa<sub>0.5</sub>TiZr alloy

Table 1  
Chemical compositions (in at.%) of the alloys studied in this work.

Alloy	Al	Hf	Mo	Nb	Ta	Ti	Zr
AlMo <sub>0.5</sub> NbTa <sub>0.5</sub> TiZr	20.4	–	10.5	22.4	10.1	17.8	18.8
Al <sub>0.4</sub> Hf <sub>0.6</sub> NbTaTiZr	7.9	12.8	–	23.0	16.8	18.9	20.6

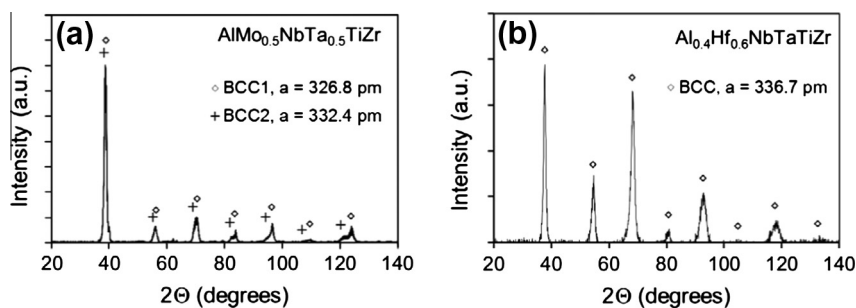


Fig. 1. X-ray diffraction patterns of the annealed cast alloys: (a)  $\text{AlMo}_{0.5}\text{NbTa}_{0.5}\text{TiZr}$  and (b)  $\text{Al}_{0.4}\text{Hf}_{0.6}\text{NbTaTiZr}$ .

(Fig. 1a). The lattice parameters of these phases are  $a_1 = 326.8$  pm and  $a_2 = 332.4$  pm, respectively (Table 2). The  $\text{Al}_{0.4}\text{Hf}_{0.6}\text{NbTaTiZr}$  alloy has a single-phase bcc crystal structure, with the lattice parameter  $a = 336.7$  pm (Fig. 1b, Table 2). No super-lattice peaks, as an evidence of crystal ordering, are observed. The density,  $\rho$ , and Vickers microhardness,  $H_v$ , values of the produced refractory alloys are given in Table 3. For the  $\text{AlMo}_{0.5}\text{NbTa}_{0.5}\text{TiZr}$  alloy,  $\rho = 7.40$  g cm $^{-3}$  and  $H_v = 5.8$  GPa, while for the  $\text{Al}_{0.4}\text{Hf}_{0.6}\text{NbTaTiZr}$  alloy,  $\rho = 9.05$  g cm $^{-3}$  and  $H_v = 4.9$  GPa.

When the crystal structure, density and microhardness of the  $\text{AlMo}_{0.5}\text{NbTa}_{0.5}\text{TiZr}$  and  $\text{Al}_{0.4}\text{Hf}_{0.6}\text{NbTaTiZr}$  alloys are compared with the properties of the parent alloys,  $\text{CrMo}_{0.5}\text{NbTa}_{0.5}\text{TiZr}$  [12] and  $\text{HfNbTaTiZr}$  [8], respectively (Tables 2 and 3), evident beneficial effects from the alloying with Al are found. Indeed, the replacement of Cr with Al eliminates the brittle Laves phase, increases microhardness from 5.3 GPa to 5.8 GPa and reduces the density from 8.23 g cm $^{-3}$  to 7.40 g cm $^{-3}$ . Similarly, partial substitution of Hf with Al considerably increases microhardness (from 3.8 to 4.9 GPa) and decreases the alloy density (from 9.94 to 9.05 g cm $^{-3}$ ), although the  $\text{Al}_{0.4}\text{Hf}_{0.6}\text{NbTaTiZr}$  alloy retains the single-phase bcc structure.

### 3.2. Compression properties

The engineering stress vs. engineering strain curves of the  $\text{AlMo}_{0.5}\text{NbTa}_{0.5}\text{TiZr}$  and  $\text{Al}_{0.4}\text{Hf}_{0.6}\text{NbTaTiZr}$  alloy samples tested at different temperatures are shown in

Table 2

The lattice parameter,  $a$  (in pm), of the cubic phases identified in the produced cast alloys, as well as in the parent alloys, (\*) after annealing and (\*\*) after compression deformation at 1273 K.

Alloy	Phase ID	$a$ (pm)*	$a$ (pm)**	Ref.
$\text{AlMo}_{0.5}\text{NbTa}_{0.5}\text{TiZr}$	bcc1	326.8	325.9	This work
	bcc2	332.4	332.2	
$\text{Al}_{0.4}\text{Hf}_{0.6}\text{NbTaTiZr}$	bcc	336.7	337.2	This work
$\text{CrMo}_{0.5}\text{NbTa}_{0.5}\text{TiZr}$	bcc1	325.5		[12]
	bcc2	338.6		
	Laves	733.4		
$\text{HfNbTaTiZr}$	bcc	340.4	340.5	[8]

Table 3

Density,  $\rho$  and microhardness,  $H_v$ , of the produced and parent alloys.

Alloy	$\rho$ (g cm $^{-3}$ )	$H_v$ (GPa)	Ref.
$\text{AlMo}_{0.5}\text{NbTa}_{0.5}\text{TiZr}$	$7.40 \pm 0.08$	$5.8 \pm 0.1$	This work
$\text{Al}_{0.4}\text{Hf}_{0.6}\text{NbTaTiZr}$	$9.05 \pm 0.05$	$4.9 \pm 0.1$	This work
$\text{CrMo}_{0.5}\text{NbTa}_{0.5}\text{TiZr}$	$8.23 \pm 0.05$	$5.3 \pm 0.1$	[12]
$\text{HfNbTaTiZr}$	$9.94 \pm 0.05$	$3.8 \pm 0.1$	[8]

Fig. 2a and b, respectively. The compression properties of these alloys, such as yield strength,  $\sigma_{0.2}$ , maximum strength,  $\sigma_p$ , elastic modulus,  $E$ , and fracture strain,  $\delta$ , are given in Tables 4 and 5, respectively. Both alloys show very high strength at room temperature (RT). The  $\text{AlMo}_{0.5}\text{NbTa}_{0.5}\text{TiZr}$  alloy has  $\sigma_{0.2} = 2000$  MPa and  $\sigma_p = 2368$  MPa, while the  $\text{Al}_{0.4}\text{Hf}_{0.6}\text{NbTaTiZr}$  alloy has  $\sigma_{0.2} = 1841$  MPa and  $\sigma_p = 2269$  MPa. The RT compression ductility of both alloys is the same,  $\delta = 10\%$ , while the elastic modulus of the  $\text{AlMo}_{0.5}\text{NbTa}_{0.5}\text{TiZr}$  ( $E = 178.6$  GPa) is considerably higher than that of the  $\text{Al}_{0.4}\text{Hf}_{0.6}\text{NbTaTiZr}$  alloy ( $E = 78.1$  GPa). With an increase in the temperature, the strengths and elastic modulus decrease, while the compression ductility increases (Tables 4 and 5). The strength decrease occurs more rapidly in the  $\text{Al}_{0.4}\text{Hf}_{0.6}\text{NbTaTiZr}$  than in  $\text{AlMo}_{0.5}\text{NbTa}_{0.5}\text{TiZr}$ . For example, at  $T = 1273$  K and 1473 K, the yield strength of the  $\text{Al}_{0.4}\text{Hf}_{0.6}\text{NbTaTiZr}$  alloy is  $\sigma_{0.2} = 745$  MPa and 250 MPa, while of the  $\text{AlMo}_{0.5}\text{NbTa}_{0.5}\text{TiZr}$  alloy is  $\sigma_{0.2} = 298$  MPa and 89 MPa, respectively. Both alloys have high compression ductility ( $\delta > 50\%$ ) at  $T = 1273$  K and 1473 K.

Fig. 3 compares the yield strength of the  $\text{AlMo}_{0.5}\text{NbTa}_{0.5}\text{TiZr}$  and  $\text{Al}_{0.4}\text{Hf}_{0.6}\text{NbTaTiZr}$  alloys with, respectively, the  $\text{CrMo}_{0.5}\text{NbTa}_{0.5}\text{TiZr}$  and  $\text{HfNbTaTiZr}$  alloys. The replacement of Cr with Al increases  $\sigma_{0.2}$  at all studied temperatures (compare  $\text{AlMo}_{0.5}\text{NbTa}_{0.5}\text{TiZr}$  and  $\text{CrMo}_{0.5}\text{NbTa}_{0.5}\text{TiZr}$ ). The effect is especially important at high temperatures. For example, at  $T = 1273$  K and 1473 K, the  $\text{CrMo}_{0.5}\text{NbTa}_{0.5}\text{TiZr}$  alloy has  $\sigma_{0.2} = 546$  MPa and 170 MPa, while the  $\text{AlMo}_{0.5}\text{NbTa}_{0.5}\text{TiZr}$  alloy has  $\sigma_{0.2} = 745$  MPa and 255 MPa, respectively, i.e. 36–50% strength increase. After partial replacement of Hf with Al, the RT yield strength almost doubles (compare  $\text{Al}_{0.4}\text{Hf}_{0.6}\text{NbTaTiZr}$  and  $\text{HfNbTaTiZr}$ ). However, the strength

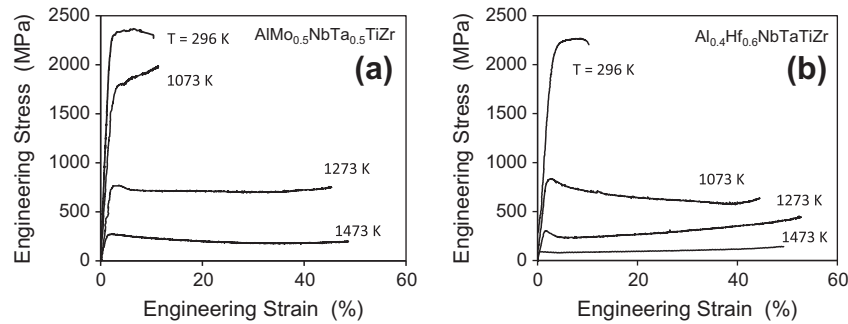


Fig. 2. Engineering stress–strain compression curves of annealed: (a)  $\text{AlMo}_{0.5}\text{NbTa}_{0.5}\text{TiZr}$  and (b)  $\text{Al}_{0.4}\text{Hf}_{0.6}\text{NbTaTiZr}$  alloys tested at different temperatures in air ( $T = 296$  K) and vacuum ( $T = 1073$ – $1473$  K).

Table 4

Compression yield strength,  $\sigma_{0.2}$ , maximum strength,  $\sigma_p$ , elastic modulus,  $E$ , and fracture strain,  $\delta$ , of the  $\text{AlMo}_{0.5}\text{NbTa}_{0.5}\text{TiZr}$  alloy at different temperatures.

$T$ (K)	296	1073	1273	1473
$\sigma_{0.2}$ (MPa)	2000	1597	745	250
$\sigma_p$ (MPa)	2368	1810	772	275
$E$ (GPa)	178.6	80	36	27
$\delta$ (%)	10	11	>50	>50

Table 5

Compression yield strength,  $\sigma_{0.2}$ , maximum strength,  $\sigma_p$ , elastic modulus,  $E$ , and fracture strain,  $\delta$ , of the  $\text{Al}_{0.4}\text{Hf}_{0.6}\text{NbTaTiZr}$  alloy at different temperatures.

$T$ (K)	296	1073	1273	1473
$\sigma_{0.2}$ (MPa)	1841	796	298	89
$\sigma_p$ (MPa)	2269	834	455	135
$E$ (GPa)	78.1	48.8	23.3	
$\delta$ (%)	10	>50	>50	>50

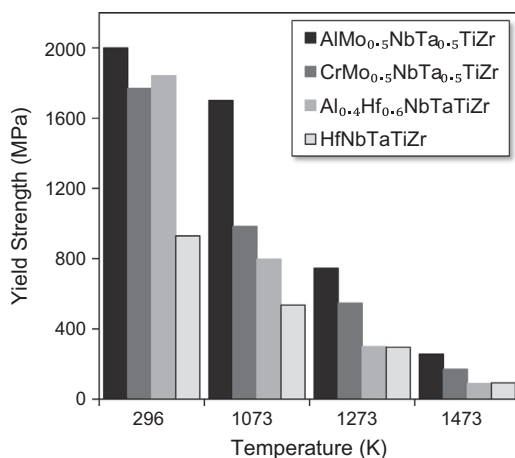


Fig. 3. Comparison of the yield strength of the  $\text{AlMo}_{0.5}\text{NbTa}_{0.5}\text{TiZr}$ ,  $\text{CrMo}_{0.5}\text{NbTa}_{0.5}\text{TiZr}$ ,  $\text{Al}_{0.4}\text{Hf}_{0.6}\text{NbTaTiZr}$  and  $\text{HfNbTaTiZr}$  alloys tested at  $T = 296$  K, 1073 K, 1273 K and 1473 K.

difference decreases with an increase in temperature, and no effect from the Al addition is seen for this alloy pair at  $T = 1273$  K and 1473 K (see Fig. 3).

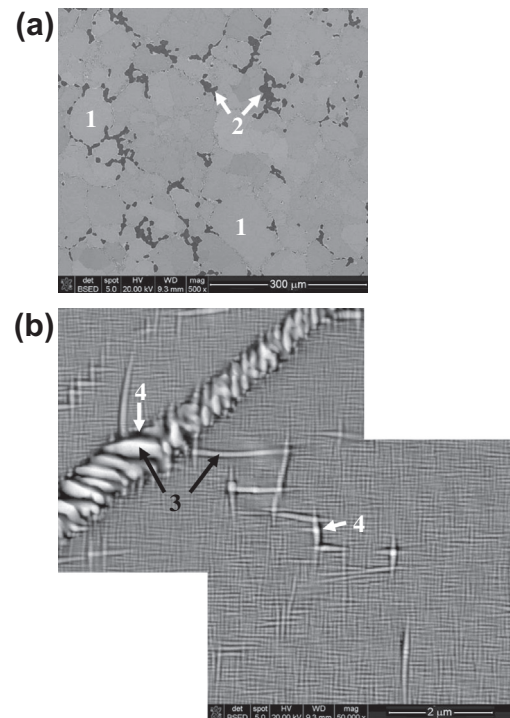


Fig. 4. Backscatter electron images of the microstructure of the annealed  $\text{AlMo}_{0.5}\text{NbTa}_{0.5}\text{TiZr}$  alloy: (a) equiaxed grain structure with dark-color second-phase particles precipitated at grain boundaries; (b) basket-like lamellar structure inside grains and at grain boundaries. Numbers and respective arrows indicate typical regions used for chemical analysis (see Table 6).

### 3.3. Microstructure

#### 3.3.1. Annealed condition

Representative SEM backscatter images of the  $\text{AlMo}_{0.5}\text{NbTa}_{0.5}\text{TiZr}$  alloy after annealing at 1673 K for 24 h and slow cooling are shown in Fig. 4. The alloy consists of a polycrystalline matrix with average grain size of  $75 \pm 5$   $\mu\text{m}$  and second-phase particles (darker material in Fig. 4a) precipitated at grain boundaries. The volume fraction of these second-phase particles is  $v_f = 11.5 \pm 1.5\%$ . EDS analysis (Table 6) shows that the average composition of the matrix grains (identified as #1 in Fig. 4a and Table 6) is very close to the overall composition of the

Table 6  
Chemical compositions (in at.%) of the  $\text{AlMo}_{0.5}\text{NbTa}_{0.5}\text{TiZr}$  alloy constituents (shown in Fig. 4) in the annealed condition.

ID #	Constituent	Al	Mo	Nb	Ta	Ti	Zr
1	Matrix grains	19.9	11.3	22.9	10.6	18.5	16.8
2	Dark large particles (at grain boundaries)	39.5	0.0	10.9	2.3	7.2	40.1
3	Bright nano-lamellar phase	15.4	14.5	25.6	12.8	19.2	12.5
4	Dark nano-lamellar phase	27.6	6.8	19.1	7.2	15.2	24.1

$\text{AlMo}_{0.5}\text{NbTa}_{0.5}\text{TiZr}$  alloy (compare Tables 6 and 1), while the dark particles (identified as #2) are enriched with Al and Zr. Higher magnification images reveal the presence of very fine, basket-like lamellar structure inside the grains (Fig. 4b). The average lamellar spacing inside the grains is estimated to be  $70 \pm 5$  nm. The lamellae coarsen at grain boundaries and reveal the presence of two phases with distinct Z contrasts. Namely, the BSE contrast of one phase is bright, which is an indication that this phase contains larger amounts of heavier elements, and another phase is dark, which is an indication that this phase mainly consists of lighter elements. The EDS analysis shows that the lamellae of the bright phase (similar to those identified as #3 in Fig. 4b) are enriched with Mo, Nb and Ta (relative to the average alloy composition), while the lamellae of the dark phase (identified as #4) are enriched with Al and Zr (Table 6). These EDS data should, however, be interpreted as an estimate of the differences in composition of these two phases, because X-ray emission volume, at the electron beam size of 3–4 nm and accelerating voltage of 15 kV, is estimated to be above  $\sim 100$  nm in diameter in this alloy [17,18], and the adjacent lamellae of another phase contribute to the intensity of the collected EDS peaks. Therefore, the measured compositions of the lamellae of the dark and bright phases are somewhat between the actual compositions of these phases. Taking into account that the X-ray diffraction shows the presence of only two phases, it is reasonable to suggest that the large dark particles at grain boundaries and nanometer-sized dark lamellae inside the grains are of the same phase and thus have the same composition. Because the two phases (bright and dark on the BSE images) have the same bcc crystal structure with very close lattice parameters (see Table 2) we were unable to identify which phase is bcc1 and which is bcc2.

After annealing at 1473 K for 24 h, the single-phase  $\text{Al}_{0.4}\text{Hf}_{0.6}\text{NbTaTiZr}$  alloy has an equiaxed grain structure (Fig. 5a). The average grain size is  $140 \pm 10$   $\mu\text{m}$ . Slight etching reveals the presence of finer subgrain structure inside the grains (Fig. 5b). Black dots seen inside the grains in Fig. 5b correspond to etched sub-grain boundaries.

### 3.3.2. Microstructure after compression deformation at 1273 K

The microstructure of the  $\text{AlMo}_{0.5}\text{NbTa}_{0.5}\text{TiZr}$  alloy after 50% compression deformation at  $T = 1273$  K is shown in Fig. 6. The alloy constituents present in the annealed condition are retained after the deformation. The matrix grains are slightly elongated in the directions

of local plastic flow, which are inclined by  $\sim 90$ – $60^\circ$  to the compression direction, and dark second-phase particles remain present at grain boundaries (Fig. 6a). The volume fraction of these particles is  $v_f = 9.0 \pm 1.0\%$ , i.e. slightly smaller than before the deformation. A characteristic relief forms inside the grains (Fig. 6b). This relief is likely a result of interaction of the local material flow with the interface boundaries between two nano-lamellar phases. After the deformation, the lamellar structure inside the matrix grains and at grain boundaries becomes coarser (Fig. 6b and c). Additionally, submicron-sized regions (spots), in which the nano-lamellar structure disappears, form inside many grains (Fig. 6d). The chemical composition of the alloy constituents is given in Table 7. After deformation, the average composition of grains (#1 in Fig. 6a and Table 7) does not change and only minor changes in the composition of the dark-color large second-phase particles (#2 in Fig. 6a and Table 7) are detected. At the same time, the coarsened nano-lamellae of the bright phase (#3 in Fig. 6b and 6c and in Table 7) become more enriched with Mo and Nb and slightly depleted of Al and Zr (in comparison with the annealed state). Coarsened nano-lamellae of the dark phase (#4 in Fig. 6 and Table 7) are more enriched with Al and Zr and depleted of other elements (compare Tables 6 and 7) and their composition becomes closer to the composition of the dark-color large second-phase particles (#2) located at grain boundaries. This observation seems to support our earlier suggestion that the large dark particles at grain boundaries and nanometer-sized dark lamellae inside the grains are the same phase and thus have the same composition. The composition of newly formed gray spots is very close to the average composition of grains and differs only by a slightly smaller concentration of Mo and a higher concentration of Ti.

Fig. 7 shows the microstructure of the  $\text{Al}_{0.4}\text{Hf}_{0.6}\text{NbTaTiZr}$  alloy after 50% compression deformation at  $T = 1273$  K. Grains become elongated in the directions of plastic flow (Fig. 7a) and deformation bands crossing some grain boundaries can be observed (Fig. 7b). Characteristic bands and spots with different contrasts are present inside the deformed grains. These distinctive contrasts inside the grains are likely caused by different electron channeling conditions and indicate the presence of a subgrain structure and internal stresses, which lead to slight misorientations of the regions inside the deformed grains [19]. Fine recrystallized grains, the average size of which is  $\sim 1.3$   $\mu\text{m}$ , are formed at grain boundaries of deformed grains (Fig. 7c and d). The chemical compositions of the recrystallized

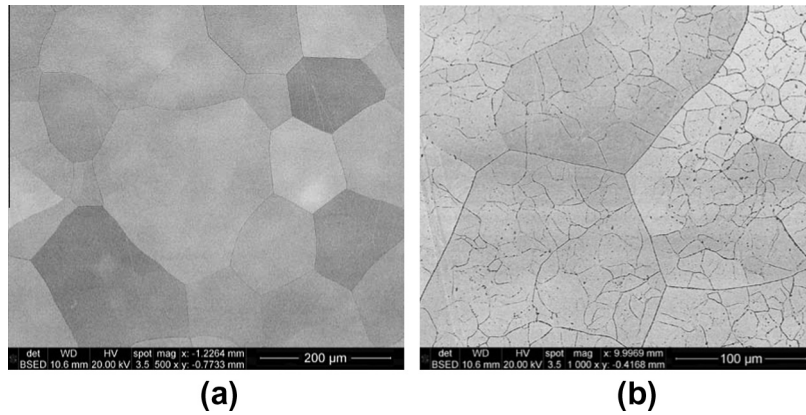


Fig. 5. (a) Equiaxed grain structure of the annealed  $\text{Al}_{0.4}\text{Hf}_{0.6}\text{NbTaTiZr}$  alloy; (b) sub-grain structure inside the grains revealed after slight etching.

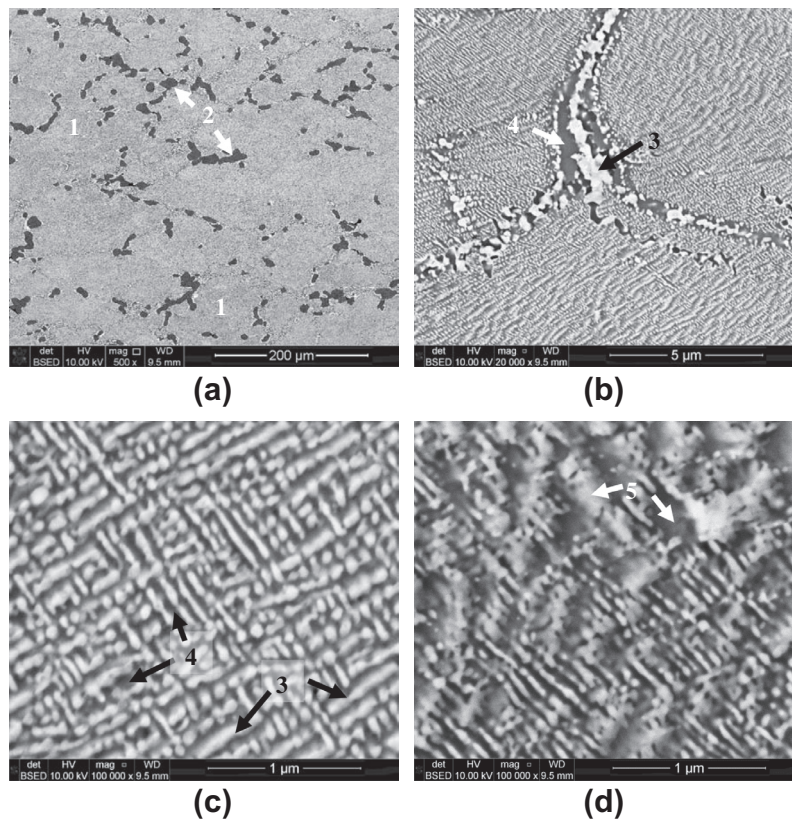


Fig. 6. Backscatter electron images of the microstructure of the  $\text{AlMo}_{0.5}\text{NbTa}_{0.5}\text{TiZr}$  alloy after compression deformation at 1000 °C: (a) low-magnification image showing deformed grains and dark-color second-phase particles at grain boundaries; (b) a junction of three grains with different fine morphologies of the two phases inside the grains; (c,d) two-phase basket-like structure inside the grains. Numbers and respective arrows indicate typical regions used for chemical analysis (see Table 7).

Table 7

Chemical compositions (in at.%) of the  $\text{AlMo}_{0.5}\text{NbTa}_{0.5}\text{TiZr}$  alloy constituents (shown in Fig. 6) after compression deformation at 1273 K.

ID #	Constituent	Al	Mo	Nb	Ta	Ti	Zr
1	Matrix grains	20.8	11.6	21.9	8.7	18.2	18.8
2	Dark large particles (at grain boundaries)	38.9	0.5	11.6	2.5	7.5	39.0
3	Bright nano-lamellar phase	12.1	18.1	27.1	13.2	18.8	10.6
4	Dark nano-lamellar phase	32.6	4.5	15.3	4.9	12.7	30.0
5	Gray regions (inside grains, Fig. 6d)	21.7	7.2	23.2	7.8	21.3	18.9

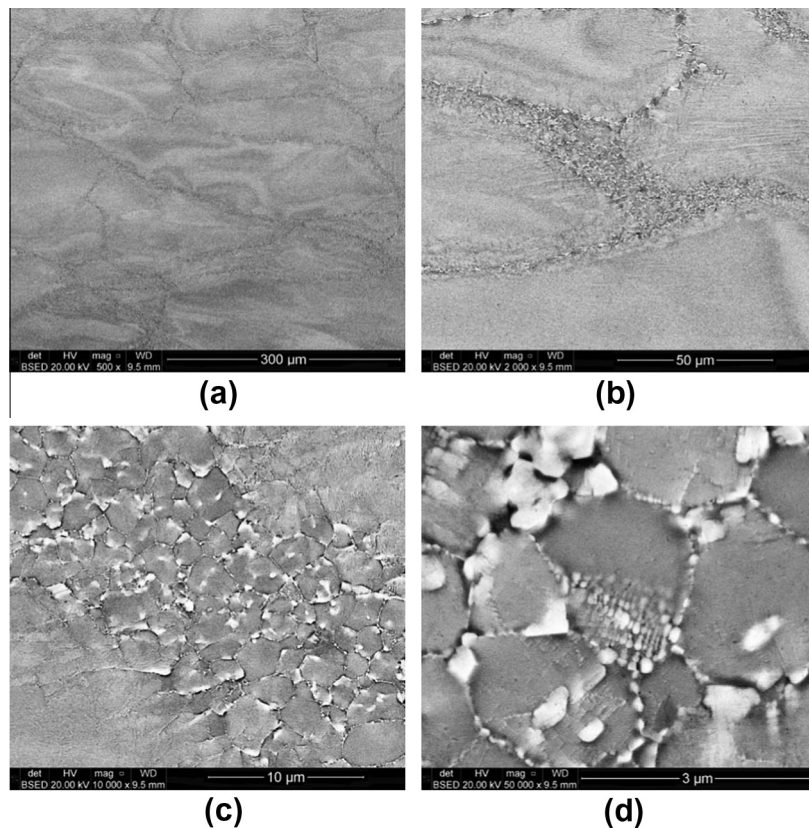


Fig. 7. Backscatter electron images of the microstructure of the  $\text{Al}_{0.4}\text{Hf}_{0.6}\text{NbTaTiZr}$  alloy after compression deformation at 1000 °C: (a and b) deformed grains with (a) characteristic channeling contrast bands inside the grains due to crystal lattice distortions and (b) deformation bands crossing a grain boundary; (c) fine recrystallized grains formed at grain boundaries; (d) a higher magnification image shows the presence of nano-precipitates at the boundaries of the recrystallized grains.

and non-recrystallized grains are the same as the average composition of the alloy (Table 1). A higher magnification image (Fig. 7d) shows the presence of nano-precipitates at the boundaries of the recrystallized grains. Their small size does not allow chemical analysis.

Fig. 8 shows X-ray diffraction patterns of the  $\text{AlMo}_{0.5}\text{NbTa}_{0.5}\text{TiZr}$  and  $\text{Al}_{0.4}\text{Hf}_{0.6}\text{NbTaTiZr}$  alloys after 50% compression deformation at 1273 K. The diffraction peaks from the deformed  $\text{AlMo}_{0.5}\text{NbTa}_{0.5}\text{TiZr}$  alloy sample become sharper and the presence of two bcc phases is clearly seen (Fig. 8a). The lattice parameter of the bcc1 phase slightly decreases from  $a_1 = 326.8$  pm in the annealed condition to  $a_1 = 325.9$  pm after deformation, while the lattice parameter of the bcc2 phase does not change and is  $a_2 = 332.2$  pm. These results taken with the

above described changes in the compositions of the bright and dark particles suggest that the bright-color particles are the bcc1 phase while the dark-color particles are the bcc2 phase. However, additional transmission electron microscopy studies are required to verify this suggestion. After the compression deformation at 1273 K, the  $\text{Al}_{0.4}\text{Hf}_{0.6}\text{NbTaTiZr}$  alloy retains the single-phase bcc structure (Fig. 8b). The lattice parameter of the bcc phase before and after deformation is almost the same in this alloy ( $a = 336.7$  pm and 337.2 pm, respectively).

### 3.4. Thermodynamic analysis

The phase diagrams for the studied complex alloys are currently unavailable. Therefore, an attempt has been

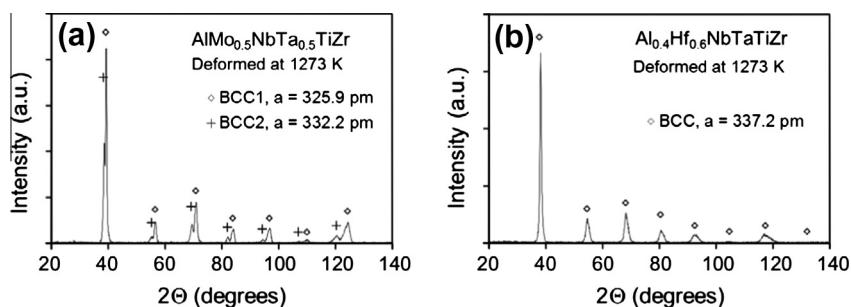


Fig. 8. X-ray diffraction patterns of the (a)  $\text{AlMo}_{0.5}\text{NbTa}_{0.5}\text{TiZr}$  and (b)  $\text{Al}_{0.4}\text{Hf}_{0.6}\text{NbTaTiZr}$  alloys after 50% compression deformation at 1273 K.

made in this work to calculate the solidification curves and equilibrium phase diagrams for these alloys. The calculation was conducted using commercial thermodynamic software Pandat™, version 8.0 [20], and the PanTi thermodynamic database developed by CompuTherm, LLC [21].

### 3.4.1. Non-equilibrium (NE) solidification modeling

NE solidification was simulated using a Scheil model, which assumes equilibrium at the interface of the solid and liquid phases, no back diffusion in solid state and no concentration gradient in the liquid phase [22,23]. The temperature dependences of the volume fractions of the solid phases formed during solidification of the studied alloys,  $\text{AlMo}_{0.5}\text{NbTa}_{0.5}\text{TiZr}$  and  $\text{Al}_{0.4}\text{Hf}_{0.6}\text{NbTaTiZr}$ , as well as parent alloys,  $\text{CrMo}_{0.5}\text{NbTa}_{0.5}\text{TiZr}$  and  $\text{HfNbTaTiZr}$ , are shown in Fig. 9. The solidification starts by the formation of a disordered bcc phase in all four alloys. A very small amount,  $\sim 0.3\%$ , of the  $\text{Al}_2\text{Zr}_3$  phase forms in  $\text{AlMo}_{0.5}\text{NbTa}_{0.5}\text{TiZr}$  and  $\sim 5.1\%$  of the Cr-rich Laves phase forms in  $\text{CrMo}_{0.5}\text{NbTa}_{0.5}\text{TiZr}$  at the end of solidification (Fig. 9a and c). A single bcc phase is predicted in the  $\text{Al}_{0.4}\text{Hf}_{0.6}\text{NbTaTiZr}$  and  $\text{HfNbTaTiZr}$  alloys after solidification (Fig. 9b and d).

The temperatures of start,  $T_L^{\text{NE}}$ , and completion,  $T_S^{\text{NE}}$ , of NE solidification, as well as the temperature of the start of formation of the second phase,  $T_2^{\text{NE}}$  (in  $\text{AlMo}_{0.5}\text{NbTa}_{0.5}\text{TiZr}$  and  $\text{CrMo}_{0.5}\text{NbTa}_{0.5}\text{TiZr}$ ) are given in Table 8. Solidification of the  $\text{AlMo}_{0.5}\text{NbTa}_{0.5}\text{TiZr}$  alloy starts at  $T_L^{\text{NE}} = 2046$  K and ends at  $T_S^{\text{NE}} = 1314$  K, with the solidification range  $\Delta T_L = T_L^{\text{NE}} - T_S^{\text{NE}} = 732$  K. The second  $\text{Al}_2\text{Zr}_3$  phase starts to form in this alloy at 1391 K. Solidification

Table 8

The temperatures of the start,  $T_L^{\text{NE}}$ , and the end,  $T_S^{\text{NE}}$ , of solidification and the start of the formation of the second phase,  $T_2^{\text{NE}}$ .

Alloy	$T_L^{\text{NE}}$ (K)	$T_S^{\text{NE}}$ (K)	$T_2^{\text{NE}}$ (K)
$\text{AlMo}_{0.5}\text{NbTa}_{0.5}\text{TiZr}$	2046	1314	1391
$\text{Al}_{0.4}\text{Hf}_{0.6}\text{NbTaTiZr}$	2238	1595	–
$\text{CrMo}_{0.5}\text{NbTa}_{0.5}\text{TiZr}$	2877	1610	1664
$\text{HfNbTaTiZr}$	2290	1836	–

of the  $\text{Al}_{0.4}\text{Hf}_{0.6}\text{NbTaTiZr}$  alloy occurs at slightly higher temperatures, i.e. it starts at 2238 K and ends at 1595 K, with  $\Delta T_L = 643$  K. Solidification of the  $\text{CrMo}_{0.5}\text{NbTa}_{0.5}\text{TiZr}$  alloy starts at 2877 K and ends at 1610 K. The solidification range for this alloy is rather high,  $\Delta T_L = 1267$  K, mainly due to a slow increase in the volume fraction of the bcc phase in the temperature range from  $T_L$  down to  $\sim 2250$  K (see Fig. 9c). The formation of the Laves phase occurs at almost constant temperature, indicating a eutectic-type reaction. Solidification of the  $\text{HfNbTaTiZr}$  alloy starts at 2290 K and ends at 1836 K, providing the narrowest solidification range  $\Delta T_L = 454$  K.

When the solidification behavior of the two Al-containing alloys,  $\text{AlMo}_{0.5}\text{NbTa}_{0.5}\text{TiZr}$  and  $\text{Al}_{0.4}\text{Hf}_{0.6}\text{NbTaTiZr}$ , are compared with that of the respective parent alloys,  $\text{CrMo}_{0.5}\text{NbTa}_{0.5}\text{TiZr}$  and  $\text{HfNbTaTiZr}$ , it can be found that the replacement of Cr with Al results in a considerable decrease in the temperatures of the start (by 831 K) and the end (by 296 K) of solidification, and also in a decrease in  $\Delta T_L$  from 1267 K for  $\text{CrMo}_{0.5}\text{NbTa}_{0.5}\text{TiZr}$  to 732 K for  $\text{AlMo}_{0.5}\text{NbTa}_{0.5}\text{TiZr}$ . At the same time, partial substitution of Hf with Al results in a decrease in  $T_L^{\text{NE}}$  by 52 K and  $T_S^{\text{NE}}$  by 241 K, which increases  $\Delta T_L$  by 189 K.

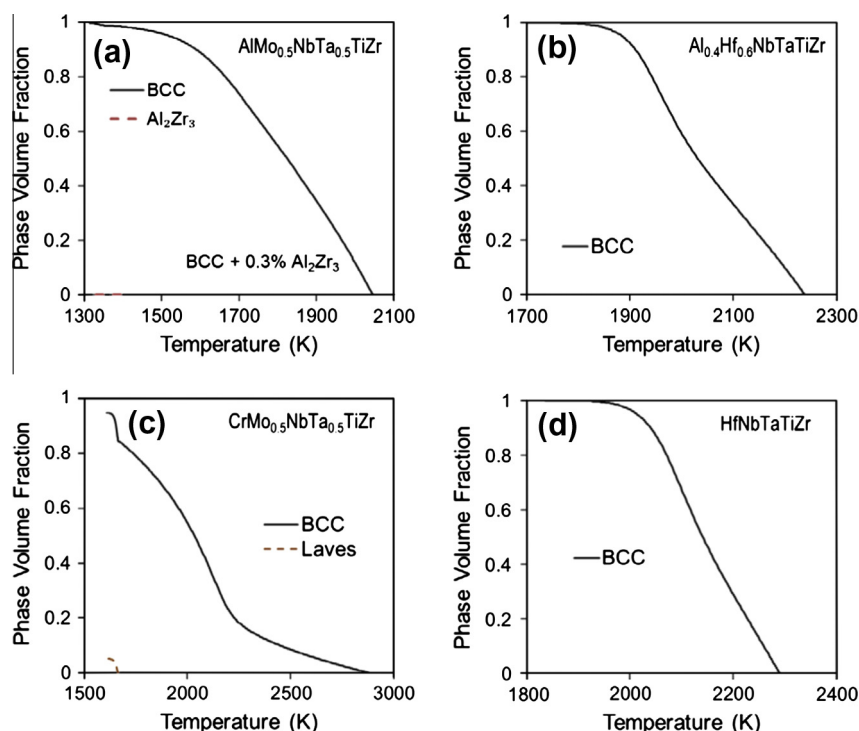


Fig. 9. Simulated solidification curves for the (a)  $\text{AlMo}_{0.5}\text{NbTa}_{0.5}\text{TiZr}$ , (b)  $\text{Al}_{0.4}\text{Hf}_{0.6}\text{NbTaTiZr}$ , (c)  $\text{CrMo}_{0.5}\text{NbTa}_{0.5}\text{TiZr}$  and (d)  $\text{HfNbTaTiZr}$  alloys.

### 3.4.2. Equilibrium phase diagrams

The simulated equilibrium phase diagrams of the four alloys are given in Fig. 10 and characteristic equilibrium phase transformation temperatures and reaction equations are given in Table 9. Equilibrium solidification occurs in a much narrower temperature range than NE solidification and results in the formation of a disordered bcc1 phase in these alloys. The single-phase bcc1 region is the widest in HfNbTaTiZr ( $\Delta T_{bcc1} = 873$  K) and the narrowest in CrMo<sub>0.5</sub>NbTa<sub>0.5</sub>TiZr ( $\Delta T_{bcc1} = 371$  K). In AlMo<sub>0.5</sub>NbTa<sub>0.5</sub>TiZr and Al<sub>0.4</sub>Hf<sub>0.6</sub>NbTaTiZr, this region is 660 K and 703 K, respectively. With decreasing temperature below 1131 K and 1068 K, the bcc1 phase in the AlMo<sub>0.5</sub>NbTa<sub>0.5</sub>TiZr alloy is computed to partially transform to Ti<sub>3</sub>Al- and Al<sub>2</sub>Zr<sub>3</sub>-based intermetallic phases, respectively (Fig. 10a). In the Al<sub>0.4</sub>Hf<sub>0.6</sub>NbTaTiZr alloy, the bcc1 phase partially transforms to disordered bcc2 (at  $T \leq 1318$  K) and hexagonal close packed (hcp, at  $T \leq 1290$  K) phases (Fig. 10b). The Laves phase in the CrMo<sub>0.5</sub>NbTa<sub>0.5</sub>TiZr alloy is predicted to be present at  $T \leq 1542$  K (Fig. 10c). Finally, complete transformation of the bcc1 phase into disordered bcc2 and hcp phases occurs in the HfNbTaTiZr alloy in the temperature range from 1258 K to 992 K, thus predicting two-phase structure, bcc2 and hcp, at  $T \leq 992$  K.

The calculated volume fractions and compositions of the equilibrium phases in the studied alloys at  $T = 1273$  K and  $T = 973$  K are given in Tables 10 and 11, respectively. At  $T = 1273$  K, the AlMo<sub>0.5</sub>NbTa<sub>0.5</sub>TiZr and HfNbTaTiZr alloys are single phase bcc1 structures, the Al<sub>0.4</sub>Hf<sub>0.6</sub>NbTaTiZr alloy contains three phases, bcc1, bcc2 and hcp, with

the volume fractions of 0.63, 0.37 and 0.01, respectively, and the CrMo<sub>0.5</sub>NbTa<sub>0.5</sub>TiZr alloy contains two phases, bcc1 and Laves, at the volume fractions of 0.8 and 0.2, respectively. In Al<sub>0.4</sub>Hf<sub>0.6</sub>NbTaTiZr, the bcc1 phase is depleted by Nb and Ta, the bcc2 phase is enriched with Nb and Ta and depleted by Al and Hf and the hcp phase is enriched with Hf and Al. In the CrMo<sub>0.5</sub>NbTa<sub>0.5</sub>TiZr alloy, the bcc1 phase is slightly enriched with Nb and Ti and depleted by Cr and Zr, while the Laves phase is essentially a binary Cr<sub>2</sub>Zr phase. The composition of the bcc1 phase in AlMo<sub>0.5</sub>NbTa<sub>0.5</sub>TiZr and HfNbTaTiZr corresponds to the composition of the respective alloy (see Table 10).

At  $T = 973$  K, the AlMo<sub>0.5</sub>NbTa<sub>0.5</sub>TiZr alloy contains three phases, bcc1, Ti<sub>3</sub>Al and Al<sub>2</sub>Zr<sub>3</sub>, at the volume fractions of 0.64, 0.24 and 0.12, respectively. The bcc1 phase is slightly enriched with Mo, Nb and Ta, the Ti<sub>3</sub>Al-based is essentially ternary Ti<sub>2</sub>ZrAl phase and Al<sub>2</sub>Zr<sub>3</sub> is the binary phase with 40% Al and 60% Zr. The Al<sub>0.4</sub>Hf<sub>0.6</sub>NbTaTiZr alloy also contains three phases, bcc1, bcc2 and hcp, at the volume fractions of 0.44, 0.42 and 0.13, respectively. The bcc1 phase is enriched with Ti and Zr, the bcc2 phase is enriched with Nb and Ta and the hcp phase is enriched with Al and Hf. The CrMo<sub>0.5</sub>NbTa<sub>0.5</sub>TiZr alloy has two phases, bcc1 and Laves, with the volume fractions of 0.71 and 0.29. The bcc1 phase is enriched with Mo, Nb and Ti, and the Laves phase is essentially a binary Cr<sub>2</sub>Zr phase. The HfNbTaTiZr alloy consists of 51% bcc2 and 49% hcp. The bcc2 phase is enriched with Nb and Ta and the hcp phase is enriched with Hf, Ti and Zr (see Table 11).

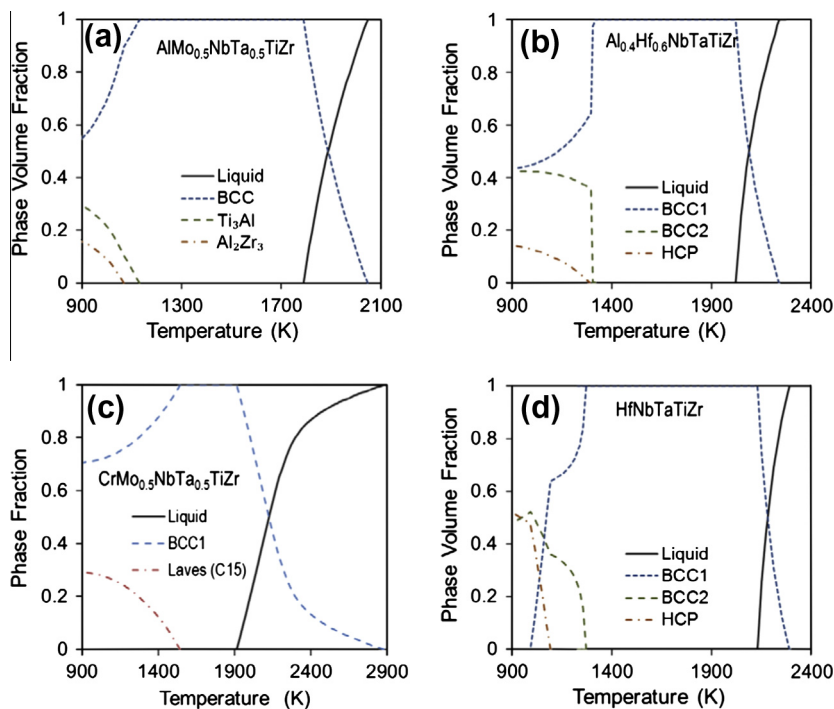


Fig. 10. Simulated equilibrium phase diagrams for the (a) AlMo<sub>0.5</sub>NbTa<sub>0.5</sub>TiZr, (b) Al<sub>0.4</sub>Hf<sub>0.6</sub>NbTaTiZr, (c) CrMo<sub>0.5</sub>NbTa<sub>0.5</sub>TiZr and (d) HfNbTaTiZr alloys.

Table 9

Characteristic equilibrium phase transformation temperatures (in K) and respective reaction equations in the studied alloys. Simulated results.

Reaction equation	AlMo <sub>0.5</sub> NbTa <sub>0.5</sub> TiZr	Al <sub>0.4</sub> Hf <sub>0.6</sub> NbTaTiZr	CrMo <sub>0.5</sub> NbTa <sub>0.5</sub> TiZr	HfNbTaTiZr
L → bcc1 ( $T_L$ )	2046	2238	2877	2290
L → bcc1 ( $T_S$ )	1791	2021	1913	2131
bcc1 → bcc2	–	1318	–	1258
bcc1 → bcc2 + hcp	–	1290	–	1092, 992
bcc1 → Laves	–	–	1542	–
bcc1 → Ti <sub>3</sub> Al	1131	–	–	–
bcc1 → Ti <sub>3</sub> Al + Al <sub>2</sub> Zr <sub>3</sub>	1068	–	–	–

Table 10

Calculated volume fractions and compositions (in at.%) of equilibrium phases in the studied alloys at  $T = 1273$  K.

$T = 1273$ K	Fraction	Al or Cr	Hf or Mo	Nb	Ta	Ti	Zr
<i>AlMo<sub>0.5</sub>NbTa<sub>0.5</sub>TiZr</i>							
bcc1	1.00	20	10	20	10	20	20
<i>Al<sub>0.4</sub>Hf<sub>0.6</sub>NbTaTiZr</i>							
bcc1	0.63	9.4	15.1	15.4	13.9	21.8	24.3
bcc2	0.37	5.2	5.5	28.3	30.9	17.3	12.9
hcp	0.01	22.4	63.1	0.1	0.1	4.8	9.5
<i>CrMo<sub>0.5</sub>NbTa<sub>0.5</sub>TiZr</i>							
bcc1	0.80	8.4	12.5	25.0	12.5	24.8	16.8
Laves	0.20	66.5	0.0	0.0	0.0	0.6	33.0
<i>HfNbTaTiZr</i>							
bcc1	1		20.0	20.0	20.0	20.0	20.0

Table 11

Calculated volume fractions and compositions (in at.%) of equilibrium phases in the studied alloys at  $T = 973$  K.

$T = 973$ K	Fraction	Al or Cr	Hf or Mo	Nb	Ta	Ti	Zr
<i>AlMo<sub>0.5</sub>NbTa<sub>0.5</sub>TiZr</i>							
bcc1	0.64	14.5	15.5	30.3	14.8	11.8	13.1
Ti <sub>3</sub> Al	0.24	25.1	0.3	2.3	2.1	51.1	19.2
Al <sub>2</sub> Zr <sub>3</sub>	0.12	40.0					60.0
<i>Al<sub>0.4</sub>Hf<sub>0.6</sub>NbTaTiZr</i>							
bcc1	0.44	8.4	7.2	10.9	6.5	30.5	36.5
bcc2	0.42	2.9	0.7	35.8	40.4	14.1	6.2
hcp	0.13	22.9	64.3	0.0	0.0	3.6	9.2
<i>CrMo<sub>0.5</sub>NbTa<sub>0.5</sub>TiZr</i>							
bcc1	0.71	1.2	14.0	28.1	14.0	28.1	14.6
Laves	0.29	66.6	0.0	0.0	0.0	0.1	33.4
<i>HfNbTaTiZr</i>							
bcc2	0.51	–	3.3	38.3	38.4	15.5	4.5
hcp	0.49	–	37.6	0.8	0.6	24.7	36.3

## 4. Discussion

### 4.1. Effect of Al additions on microstructure and properties

The results of this work demonstrate that the addition of Al to refractory HEAs have several beneficial effects. First, being much lighter than any of the refractory elements, Al considerably reduces the alloy density. For example, complete substitution of Cr with Al in CrMo<sub>0.5</sub>NbTa<sub>0.5</sub>TiZr reduces the density by 10.1%; partial (40%) substitution of Hf with Al in HfNbTaTiZr reduces the alloy density by 9.0%. Second, the addition of Al results in an increase in the RT hardness

and strength of refractory HEAs. For example, RT hardness and yield strength of AlMo<sub>0.5</sub>NbTa<sub>0.5</sub>TiZr are 9.4% and 12.7% higher than of CrMo<sub>0.5</sub>NbTa<sub>0.5</sub>TiZr. RT hardness and yield strength of Al<sub>0.4</sub>Hf<sub>0.6</sub>NbTaTiZr are 28.9% and 84.8% higher than the respective properties of HfNbTaTiZr.

A similar strengthening effect from the Al addition was earlier reported in the Co–Cr–Cu–Fe–Ni HEA system and was related to the transformation of a softer fcc phase to stronger bcc phase with an increase in the concentration of Al [1,24,25]. In our case, however, the Al-induced strengthening in the Al<sub>x</sub>Hf<sub>1–x</sub>NbTaTiZr system occurs

without any evidence of phase transformation and the alloys with  $X=0$  and  $X=0.4$  have similar single phase bcc crystal structures. Moreover, the average grain size in these alloys is also the same [8]. Therefore, the Al-induced strengthening mechanism in the  $\text{Al}_x\text{Hf}_{1-x}\text{NbTaTiZr}$  alloy system is not related to the phase changes. One may suggest that it can be caused by the formation of stronger interatomic bonds, as Al has strong bonding to each of the alloying elements (see below). The rapid decrease in the difference between the strengths of the  $\text{Al}_{0.4}\text{Hf}_{0.6}\text{NbTaTiZr}$  and  $\text{HfNbTaTiZr}$  alloys with an increase in temperature can then be explained by rapid weakening of the Al–TM bonds. The first-principles calculations are, however, required to verify the proposed scenario.

At the same time, the  $\text{AlMo}_{0.5}\text{NbTa}_{0.5}\text{TiZr}$  alloy consists of a very fine nano-scale mixture of two (likely coherent) phases, bcc1 and bcc2, at near equal volume fractions, while the parent  $\text{CrMo}_{0.5}\text{NbTa}_{0.5}\text{TiZr}$  alloy consists of three relatively coarse-grained phases, bcc1, bcc2 and Laves, at the volume fractions of 67%, 16% and 17%, respectively [12]. Therefore, the Al-induced strengthening in this alloy system can be due to both stronger interatomic bonds and much more developed interface boundaries between the phases, which impede deformation flow. Due to high thermal stability of the two-phase nanostructure, the  $\text{AlMo}_{0.5}\text{NbTa}_{0.5}\text{TiZr}$  alloy retains its high strength at temperatures up to 1473 K, and the difference in the strengths of this alloy and the parent Cr-containing alloy increases with an increase in temperature.

Additional advantage from the replacement of Cr with Al in the refractory HEAs is suppression or complete elimination of the formation of a brittle, topologically close-packed Laves phase. The formation of such a Laves phase is favored by the presence of two types of atoms with the atom size ratio close to  $\sqrt{3/2} \approx 1.225$  [26]. Among the refractory elements, Cr has the smallest atomic radius and forms binary Laves phases with Nb, Ta, Ti and Zr [27] at the atomic radius ratios of 1.14, 1.14, 1.15 and 1.25, respectively (see Table 12). At the same time, the atomic radius of Al is very close to the atomic radii of other alloying elements. The small atomic size difference between the alloying elements has recently been shown to be one of the necessary criteria favoring the formation of disordered solid solutions and discouraging the formation of intermetallic phases in HEAs [10,11,28,29]. On the other hand, Al has a different crystal structure and forms a number of binary intermetallic phases with refractory elements [27]. Therefore, it is worth understanding why the refractory HEAs containing Al do not form intermetallic phases.

Binary intermetallic phases, which are present in the binary alloy systems of the selected alloying elements, are listed in Table 13. Their enthalpies of mixing and the temperature ranges of stability are also shown there. It is seen from this table that Al can form a number of binary intermetallic phases with Hf, Mo, Nb, Ta, Ti and Zr. Other binary intermetallic phases that can form between the selected alloying elements are five Laves phases, i.e.  $\text{Mo}_2\text{Zr}$ ,  $\text{Cr}_2\text{Nb}$ ,

$\text{Cr}_2\text{Ta}$ ,  $\text{Cr}_2\text{Ti}$  and  $\text{Cr}_2\text{Zr}$ . The AlZr intermetallic phase has the largest enthalpy of formation,  $\Delta H_{\text{mix}} = -43.7 \text{ kJ mol}^{-1}$ , followed by  $\text{Al}_3\text{Zr}_2$  ( $-42.6 \text{ kJ mol}^{-1}$ ) and  $\text{Al}_2\text{Zr}_3$  ( $-41.4 \text{ kJ mol}^{-1}$ ). The large negative values mean strong bonding between the two elements, and heat is evolved when forming the compound. The enthalpies of formation of other Al–Zr intermetallics and those of Al–Hf are between  $-40$  and  $-30 \text{ kJ mol}^{-1}$  and Al–Ti intermetallics are between  $-30$  and  $-20 \text{ kJ mol}^{-1}$  (see Table 13). From Table 13, it is found that strong binary compounds form in the Al–Zr and Al–Hf binary systems, followed by those in the Al–Ti system, then in the Al–Nb binary. In comparison,  $\text{Cr}_2\text{Zr}$  has the strongest bond (with an enthalpy of formation of  $-11.3 \text{ kJ mol}^{-1}$ ) among all the binary Laves phases, but it is significantly weaker than the bonds in all the Al–Zr, Al–Hf, Al–Ti, Al–Ta and Al–Nb binary intermetallic phases. Because more negative enthalpy of formation between two elements generally indicates a higher tendency to form intermetallic phases, a number of Al-containing intermetallics should be expected in the Al-containing refractory HEAs. Surprisingly, the experimental results did not show the formation of intermetallic phases in the  $\text{AlMo}_{0.5}\text{NbTa}_{0.5}\text{TiZr}$  and  $\text{Al}_{0.4}\text{Hf}_{0.6}\text{NbTaTiZr}$  HEAs. The thermodynamic analysis also does not predict intermetallic phases in the  $\text{Al}_{0.4}\text{Hf}_{0.6}\text{NbTaTiZr}$  HEA at  $T \geq 900 \text{ K}$ , in the  $\text{AlMo}_{0.5}\text{NbTa}_{0.5}\text{TiZr}$  HEA at  $T \geq 1131 \text{ K}$  and in the  $\text{CrMo}_{0.5}\text{NbTa}_{0.5}\text{TiZr}$  HEA at  $T \geq 1542 \text{ K}$  (see Table 9). The simulation, however, calculates two intermetallic phases,  $\text{Ti}_3\text{Al}$  and  $\text{Al}_2\text{Zr}_3$ , in  $\text{AlMo}_{0.5}\text{NbTa}_{0.5}\text{TiZr}$  at  $T < 1131 \text{ K}$  and  $1068 \text{ K}$ , respectively, and a Laves  $\text{Cr}_2\text{Zr}$  phase in  $\text{CrMo}_{0.5}\text{NbTa}_{0.5}\text{TiZr}$ . It is likely that although the very negative mixing enthalpies favor the formation of intermetallic phases, other parameters of the HEAs, such as mixing entropy, atomic size difference and electronegativity difference of the alloying elements, may favor the formation of solid solution phases.

Zhang et al. and Yang and Zhang [11,30] have recently defined two parameters,  $\delta_r$  and  $\Omega$ , to predict the composition range of solid solution phase formation in HEAs. The atomic size difference parameter  $\delta_r$  is calculated using the following equation:

$$\delta_r = 100\% \sqrt{\sum c_i (1 - r_i/\bar{r})^2} \quad (1)$$

where  $c_i$  is the atomic fraction of element  $i$  in the alloy,  $\bar{r} = \sum c_i r_i$  is the average atomic radius and  $r_i$  is the atomic radius of element  $i$ . The parameter  $\Omega$  takes into account the combined effects of the mixing entropy,  $\Delta S_{\text{mix}} = -R \sum c_i \ln c_i$ , mixing enthalpy,  $\Delta H_{\text{mix}} = \sum 4\omega_{ij} c_i c_j$ , and effective melting temperature,  $T_m = \sum c_i T_{mi}$ , of a HEA and is defined as:

$$\Omega = \frac{T_m \Delta S_{\text{mix}}}{|\Delta H_{\text{mix}}|} \quad (2)$$

Here  $\omega_{ij}$  is a concentration-dependent interaction parameter between elements  $i$  and  $j$  in a sub-regular solid solution

Table 12

Metallic atomic radius,  $r$ , Pauling electronegativity,  $\chi$ , valence electron concentration,  $V$ , and melting temperature,  $T_m$ , of the elements in the studied alloys [36].

Element	Al	Cr	Hf	Mo	Nb	Ta	Ti	Zr
$r$ (pm)	143	128	159	139	146	146	147	160
$\chi$	1.61	1.66	1.3	2.16	1.60	1.50	1.54	1.33
$V$	3	6	4	6	5	5	4	4
$T_m$ (K)	933.5	2180	2506	2896	2750	3290	1941	2128

Table 13

Binary intermetallic phases, their enthalpy of mixing and temperature range of stability in given binary systems.

System	Phase	$\Delta H_{\text{mix}}$ [30] (kJ mol <sup>-1</sup> )	Temperature range [27] (K)
Al–Mo	Al <sub>12</sub> Mo	–1.45	<934
	Al <sub>5</sub> Mo	–2.83	<1008
	Al <sub>4</sub> Mo	–3.26	<1403
	Al <sub>8</sub> Mo <sub>3</sub>	–4.05	<1818
	AlMo	–5.10	1743–1993
	AlMo <sub>3</sub>	–3.83	<2423
Al–Nb	Al <sub>3</sub> Nb	–13.76	<1873
	AlNb <sub>2</sub>	–16.09	<2213
	AlNb <sub>3</sub>	–13.54	<2333
Al–Ta	Al <sub>3</sub> Ta	–14.51	<1824
	Al <sub>2</sub> Ta <sub>3</sub>	–19.20	<1867
	AlTa	–18.37	<2043
	AlTa <sub>2</sub>	–17.16	<2373
Al–Ti	Al <sub>3</sub> Ti	–22.11	<1623
	Al <sub>2</sub> Ti	–26.20	<1513
	AlTi	–29.50	<1753
	AlTi <sub>3</sub>	–22.18	<1453
Al–Zr	Al <sub>3</sub> Zr	–34.04	<1853
	Al <sub>2</sub> Zr	–39.82	<1918
	Al <sub>3</sub> Zr <sub>2</sub>	–42.57	<1868
	AlZr	–43.70	<1548
	Al <sub>2</sub> Zr <sub>3</sub>	–41.38	<1758
	AlZr <sub>2</sub>	–37.97	<1523
	AlZr <sub>3</sub>	–31.70	<1261
Al–Hf	Al <sub>3</sub> Hf	–29.89	<1863
	Al <sub>2</sub> Hf	–35.00	<1923
	Al <sub>3</sub> Hf <sub>2</sub>	–37.46	<1913
	AlHf	–38.50	<2073
	Al <sub>2</sub> Hf <sub>3</sub>	–36.50	<1863
	AlHf <sub>2</sub>	–33.52	<1393
Mo–Zr	Mo <sub>2</sub> Zr	–5.67	<2153
Cr–Nb	Cr <sub>2</sub> Nb	–6.65	<2043
Cr–Ta	Cr <sub>2</sub> Ta	–6.17	<2293
Cr–Ti	Cr <sub>2</sub> Ti	–6.47	<1643
Cr–Zr	Cr <sub>2</sub> Zr	–11.30	<1946

model [31] and  $T_{mi}$  is the melting temperature of element  $i$ . Analyzing a number of non-refractory HEAs, Yang and Zhang have found that the formation of intermetallic phases in a HEA during solidification is restricted if  $\Omega > 1.1$  and  $\delta_r < 6.6\%$  [30].

Using the atomic radii and melting temperatures of the elements given in Table 12, as well as  $\omega_{ij}$  values from Ref. [31], the parameters  $\Delta H_{\text{mix}}$ ,  $\Delta S_{\text{mix}}$ ,  $\Omega$  and  $\delta_r$  have been calculated for the four refractory HEAs, and their values are given in Table 14.  $\Delta H_{\text{mix}}$  has the maximum value of

2.7 kJ mol<sup>-1</sup> for HfNbTaTiZr and the minimum value of –17.0 kJ mol<sup>-1</sup> for AlMo<sub>0.5</sub>NbTa<sub>0.5</sub>TiZr. The CrMo<sub>0.5</sub>NbTa<sub>0.5</sub>TiZr HEA, which contains 17% of the Laves phase, has  $\Delta H_{\text{mix}} = -5.2$  kJ mol<sup>-1</sup>. It can be seen that there is no direct correlation between the  $\Delta H_{\text{mix}}$  values and the formation of the intermetallic phase. The Al- and Cr-containing alloys have the same values of  $\Delta S_{\text{mix}} = 14.5$  J mol<sup>-1</sup> K<sup>-1</sup> and HfNbTaTiZr has  $\Delta S_{\text{mix}} = 13.4$  J mol<sup>-1</sup> K<sup>-1</sup>. Thus, there is no correlation between  $\Delta S_{\text{mix}}$  and the formation of intermetallic phases

in these alloys either. At the same time, the combined parameter  $\Omega$  varies from  $\Omega = 1.7$  for  $\text{AlMo}_{0.5}\text{NbTa}_{0.5}\text{TiZr}$  to  $\Omega = 12.7$  for  $\text{HfNbTaTiZr}$ , while  $\delta_r$  is equal to 4.3% for the Hf-containing alloys, 4.5% for  $\text{AlMo}_{0.5}\text{NbTa}_{0.5}\text{TiZr}$  and 7.2% for  $\text{CrMo}_{0.5}\text{NbTa}_{0.5}\text{TiZr}$ . The  $\Omega$  criterion ( $\Omega > 1.1$ ) predicts that these four refractory alloys should form solid solution phases. On the other hand, the  $\delta_r$  criterion ( $\delta_r > 6.6\%$ ) confirms the formation of an intermetallic phase in the Cr-containing alloy. One can therefore conclude that the formation of intermetallic phases in the refractory HEAs seems to be more sensitive to the atomic size difference than to the values of the enthalpy of mixing of the alloying elements.

Table 14 also shows the values of the electronegativity difference parameter,  $\delta_\chi$ , and the valence electron concentration ( $V$ ) difference parameter,  $\delta_v$ , for the studied HEAs. The  $\delta_\chi$  and  $\delta_v$  are defined as:

$$\delta_\chi = 100\% \sqrt{\sum c_i (1 - \chi_i / \bar{\chi})^2} \quad (3)$$

$$\delta_v = 100\% \sqrt{\sum c_i (1 - V_i / \bar{V})^2} \quad (4)$$

Here  $\chi_i$  and  $V_i$  are the Pauling electronegativity and valence electron concentration, respectively, of element  $i$ ,  $\bar{\chi} = \sum c_i \chi_i$  and  $\bar{V} = \sum c_i V_i$  are the average electronegativity and valence electron concentration of the alloying elements. The  $\chi_i$  and  $V_i$  values are given in Table 12. In accordance with Hume-Rothery rules for binary substitutional solid solutions [32], the solvent and solute should have the same valency and similar electronegativity, in addition to small atomic size difference. Therefore, it is interesting to see if these rules also work for complex HEAs. The results seem to show no direct correlation between  $\delta_\chi$  and the formation of intermetallic phases. Both the  $\text{AlMo}_{0.5}\text{NbTa}_{0.5}\text{TiZr}$  and  $\text{CrMo}_{0.5}\text{NbTa}_{0.5}\text{TiZr}$  alloys have the same high value of  $\delta_\chi = 13.8\%$ , in spite of the fact that the first alloy does not form an intermetallic phase. Two Hf-containing alloys have noticeably smaller  $\delta_\chi = 7.8$ – $8.1\%$ . A similar conclusion has been drawn earlier for non-refractory HEAs [30]. We also did not find any reasonable correlation between  $\delta_v$  and the formation of intermetallic phases (see Table 14). The smallest  $\delta_v$  value of 11.1% has the single bcc phase  $\text{HfNbTaTiZr}$  and the highest  $\delta_v$  value of 20.9% has the two-phase  $\text{AlMo}_{0.5}\text{NbTa}_{0.5}\text{TiZr}$  alloy. The three-phase  $\text{CrMo}_{0.5}\text{NbTa}_{0.5}\text{TiZr}$  alloy has an intermediate value of  $\delta_v = 17.0\%$ .

## 4.2. Comparison of thermodynamic calculations with experimental data

### 4.2.1. $\text{AlMo}_{0.5}\text{NbTa}_{0.5}\text{TiZr}$

Although the thermodynamic analysis predicts two phases, bcc1 and  $\text{Al}_2\text{Zr}_3$ , after NE solidification, and three phases, bcc1,  $\text{Ti}_3\text{Al}$  and  $\text{Al}_2\text{Zr}_3$ , in the equilibrium condition, the experimental results show the presence of two bcc phases in the  $\text{AlMo}_{0.5}\text{NbTa}_{0.5}\text{TiZr}$  alloy. There is no experimental evidence for the presence of a hexagonal ( $\text{Ti}_3\text{Al}$ ) and/or tetragonal ( $\text{Al}_2\text{Zr}_3$ ) phases in this alloy at RT. Moreover, evolution of the microstructure during compression deformation at 1273 K suggests that the two bcc phases are also present at 1273 K, while the thermodynamic analysis suggests the existence of a single bcc phase at  $T > 1131$  K. At the same time, the binary Ti–Mo, Nb–Zr and Ta–Zr phase diagrams contain a wide phase separation range where the high-temperature bcc phase decomposes into two bcc phases, one of which is rich with Ti and/or Zr and another is rich with Mo, Nb, and/or Ta. For example, in the Ta–Zr system, two bcc phases are present at  $1073 \text{ K} \leq T \leq 2053 \text{ K}$  [33]. It is likely that similar phase separation also occurs in the multicomponent  $\text{AlMo}_{0.5}\text{NbTa}_{0.5}\text{TiZr}$  alloy, with one bcc phase enriched with Mo, Nb and Ta and another bcc phase enriched with Zr. The formation of the low-temperature  $\text{Ti}_3\text{Al}$  and  $\text{Al}_2\text{Zr}_3$  phases is probably restricted by slow diffusion of the alloying elements in HEAs [33].

### 4.2.2. $\text{Al}_{0.4}\text{Hf}_{0.6}\text{NbTaTiZr}$

The thermodynamic analysis predicts a single bcc phase after NE solidification, and two bcc phases and one hexagonal phase in equilibrium conditions at  $T \leq 1318$  K. The X-ray and microstructural analysis revealed the presence of only one bcc phase in this alloy, both in annealed and in hot deformed conditions. The absence of the low temperature phases can be due to sluggish diffusion of the alloying elements or to the limitation of the current PanTi thermodynamic database.

### 4.2.3. $\text{CrMo}_{0.5}\text{NbTa}_{0.5}\text{TiZr}$

A eutectic-type reaction is predicted at the end of solidification of this alloy. This result is in fairly good agreement with the experimental observations of the microstructure consisting of the large bcc1 particles (dendrites) embedded in a continuous network of the mixture of the bcc2 and

Table 14

The enthalpy of mixing,  $\Delta H_{\text{mix}}$ , entropy of mixing,  $\Delta S_{\text{mix}}$ , effective melting temperature,  $T_m$ , and parameter  $\Omega$ , as well as atomic size difference,  $\delta_r$ , electronegativity difference,  $\delta_\chi$ , and valence electron concentration difference between the alloying elements, in four HEAs.

Alloy	$\Delta H_{\text{mix}}$ (kJ mol <sup>−1</sup> )	$\Delta S_{\text{mix}}$ (J mol <sup>−1</sup> K <sup>−1</sup> )	$T_m$ (K)	$\Omega$	$\delta_r$ (%)	$\delta_\chi$ (%)	$\delta_v$ (%)	Phases
$\text{AlMo}_{0.5}\text{NbTa}_{0.5}\text{TiZr}$	−17.0	14.5	1982	1.7	4.5	13.8	20.9	bcc1 + bcc2
$\text{Al}_{0.4}\text{Hf}_{0.6}\text{NbTaTiZr}$	−6.5	14.5	2397	5.4	4.3	7.8	14.2	bcc
$\text{CrMo}_{0.5}\text{NbTa}_{0.5}\text{TiZr}$	−5.2	14.5	2418	6.8	7.2	13.8	17.0	bcc1 + bcc2 + Laves
$\text{HfNbTaTiZr}$	2.7	13.4	2523	12.7	4.3	8.1	11.1	bcc

Laves phases (inter-dendritic eutectic) [12]. At the same time, the equilibrium diagram predicts only one bcc1 phase and the formation of the Laves phase by a solid-state reaction from the bcc1 phase at  $T \leq 1542$  K, which is not supported by the experiment [12,34].

#### 4.2.4. HfNbTaTiZr

Experimental results showed a single bcc phase in this alloy in annealed condition [8]. However, precipitation of fine particles of an unidentified second phase was noticed in a narrow temperature range near 1073 K [9]. These experimental results seem to support the results of the thermodynamic analysis of this alloy.

The comparison of the simulated and experimental results for the four studied alloys indicates satisfactory agreement between the experimentally observed phases and phases predicted after NE solidification. However, noticeable disagreements of the calculated equilibrium phase diagrams with the experimentally observed phase compositions of the three alloys,  $\text{AlMo}_{0.5}\text{NbTa}_{0.5}\text{TiZr}$ ,  $\text{Al}_{0.4}\text{Hf}_{0.6}\text{NbTaTiZr}$ , and  $\text{CrMo}_{0.5}\text{NbTa}_{0.5}\text{TiZr}$ , is observed. One reason for this is that the alloys, even after 24 h annealing at 1673 or 1473 K, were still in NE conditions because of sluggish diffusion. Another explanation is that the currently available thermodynamic database is not sufficient to correctly predict phase compositions of these multi-principal-element alloys. Indeed, this database was developed by CompuTherm, LLC for Ti-rich alloys via extrapolation of the interaction parameters from the lower order constituent binary and (some) ternary systems to higher order interactions [35]. Since it is focused at the Ti-rich corner, many phases away from the Ti-rich corner are not well modeled, or even not included in the database. This database, therefore, needs further development in order to be used in the middle of the composition space for the design of HEAs.

## 5. Summary and conclusions

Compositions of two earlier reported refractory alloys, HfNbTaTiZr and  $\text{CrMo}_{0.5}\text{NbTa}_{0.5}\text{TiZr}$ , were modified to produce  $\text{Al}_{0.4}\text{Hf}_{0.6}\text{NbTaTiZr}$  and  $\text{AlMo}_{0.5}\text{NbTa}_{0.5}\text{TiZr}$  alloys, and the effect of alloying with Al on the microstructure, composition and mechanical properties of these refractory HEAs was reported. Several beneficial effects from the Al additions were found.

Complete substitution of Cr with Al in the  $\text{CrMo}_{0.5}\text{NbTa}_{0.5}\text{TiZr}$  alloy reduced the alloy density by 10.1%, increased RT hardness and yield strength by  $\sim 12\%$ , noticeably improved RT ductility and also considerably increased, by more than 50%, high-temperature strength in the temperature range from 1073 K to 1473 K. These improvements in the mechanical properties were related to dramatic changes in the phase composition and microstructure. While the  $\text{CrMo}_{0.5}\text{NbTa}_{0.5}\text{TiZr}$  alloy contained three relatively coarse phases, bcc1, bcc2 and Laves, only

two disordered bcc phases, mainly in the form of spinodal-like nano-lamellar structure, and no intermetallic phases, were present in the  $\text{AlMo}_{0.5}\text{NbTa}_{0.5}\text{TiZr}$  alloy.

Partial substitution of Hf with Al in the HfNbTaTiZr alloy reduced the alloy density by  $\sim 9\%$  and increased RT hardness and yield strength by 29% and 98%, respectively. The difference in the yield strength of the HfNbTaTiZr and  $\text{Al}_{0.4}\text{Hf}_{0.6}\text{NbTaTiZr}$  alloys, however, rapidly disappears with an increase in temperature and the properties of these two alloys were the same at 1273 K and 1473 K. Both alloys had a single-phase bcc structure with the average grain size of  $\sim 140$   $\mu\text{m}$ .

Solidification and phase equilibrium conditions of the studied alloys were calculated using the available PanTi™ (Computherm, LLC) thermodynamic database. Although satisfactory agreements between the experimentally observed phases and phases predicted after NE solidification were observed, the calculated equilibrium phase diagrams of the three alloys,  $\text{AlMo}_{0.5}\text{NbTa}_{0.5}\text{TiZr}$ ,  $\text{Al}_{0.4}\text{Hf}_{0.6}\text{NbTaTiZr}$  and  $\text{CrMo}_{0.5}\text{NbTa}_{0.5}\text{TiZr}$ , noticeably disagreed with the experimentally observed phase compositions. It was concluded that the current PanTi™ database, which was developed for the Ti-rich alloys, cannot be directly applied to the multi-principal-alloy compositions. A thermodynamic database covering the full composition range for the Al–Cr–Hf–Mo–Nb–Ta–Ti–Zr system needs to be developed to correctly predict phase equilibria and guide the design of refractory HEAs based on this system.

## Acknowledgements

Valuable discussions with Drs. Jonathan Miller, Daniel Miracle, Jay Tiley and Fan Zhang are recognized. This work was supported through the Air Force Research Laboratory Director's fund and through the Air Force on-site Contract No. FA8650-10-D-5226 conducted by UES, Inc., Dayton, Ohio.

## References

- [1] Yeh JW, Chen SK, Lin SJ, Gan JY, Chin TS, Shun TT, et al. *Adv Eng Mater* 2004;6(5):299.
- [2] Yeh JW. *Ann Chim: Sci Mater* 2006;31:633.
- [3] Yeh JW, Chen YL, Lin SJ, Chen SK. *Mater Sci Forum* 2007;560:1.
- [4] Yang X, Zhang Y. *Mater Chem Phys* 2012;132:233–8.
- [5] Zhang KB, Fu ZY. *Intermetallics* 2012;22:24–32.
- [6] Senkov ON, Wilks GB, Miracle DB, Chuang CP, Liaw PK. *Intermetallics* 2010;18:1758.
- [7] Senkov ON, Wilks GB, Scott JM, Miracle DB. *Intermetallics* 2011;19:698.
- [8] Senkov ON, Scott JM, Senkova SV, Miracle DB, Woodward CF. *J Alloys Compd* 2011;509:6043.
- [9] Senkov ON, Scott JM, Senkova SV, Meisenkothen F, Miracle DB, Woodward CF. *J Mater Sci* 2012;47:4062.
- [10] Zhang Y, Zhou YJ, Lin JP, Chen GL, Liaw PK. *Adv Eng Mater* 2008;10(6):534.
- [11] Zhang Y, Yang X, Liaw PK. *J Met* 2012;64(7):830.
- [12] Senkov ON, Woodward CF. *Mater Sci Eng A* 2011;529:311.
- [13] Senkov ON, Senkova SV, Dimiduk DM, Woodward C, Miracle DB. *J Mater Sci* 2012;47:6522.

- [14] Senkov ON, Senkova SV, Woodward C, Miracle DB. *Acta Mater* 2013;61:1545.
- [15] Senkov ON, Senkova SV, Miracle DB, Woodward CF. *Mater Sci Eng A* 2013;565:51.
- [16] He JY, Liu WH, Wang H, Wu Y, Liu XJ, Nieh TG, et al. *Acta Mater* 2013. <http://dx.doi.org/10.1016/j.actamat.2013.09.037>.
- [17] Friel JJ. X-ray and image analysis in electron microscopy. Princeton Gamma-Tech.; 1995.
- [18] Monte Carlo simulation of electron trajectory in solids, <<http://www.gel.usherbrooke.ca/casino/>>.
- [19] Newbury DE, Joy DC, Echlin P, Fiori CE, Goldstein JI. *Advanced scanning electron microscopy and X-ray microanalysis*. New York: Plenum; 1986.
- [20] Cao W, Chen SL, Zhang F, Wu K, Yang Y, Chang YA, et al. *CALPHAD* 2009;33:328.
- [21] Zhang F, Xie FY, Chen SL, Chang YA, Furrer D, Venkatesh V. *J Mater Eng Perf* 2005;14(6):717–21.
- [22] Scheil E. *Z Metallkd* 1942;34:70.
- [23] Porter DA, Easterling KE. *Phase transformations in metals and alloys*. 2nd ed. London: Chapman & Hall; 1992.
- [24] Huang PK, Yeh JW, Shun TT, Chen SK. *Adv Eng Mater* 2004;6:74.
- [25] Li C, Li JC, Zhao M, Jiang Q. *J Alloys Compd* 2010;S504:S515.
- [26] Stein F, Plam M, Sauthoff G. *Intermetallics* 2004;12:713.
- [27] Massalski TB, Okamoto H. *Binary alloy phase diagrams*. 2nd ed. Materials Park (OH): ASM International; 1990.
- [28] Zhang Y, Zhou YJ. *Mater Sci Forum* 2007;561–565:1337.
- [29] Guo S, Liu CT. *Prog Nat Sci: Mater Int* 2011;21:433.
- [30] Yang X, Zhang Y. *Mater Chem Phys* 2012;132:233.
- [31] Takeuchi A, Inoue A. *Intermetallics* 2010;18:1779.
- [32] Hume-Rothery W. *The structure of metals and alloys*. London: Institute of Metals; 1936.
- [33] Tsai KY, Tsai MH, Yeh JW. *Acta Mater* 2013;61:4887.
- [34] Senkov ON, Senkova SV, Dimiduk DM, Woodward C, Miracle DB. *J Mater Sci* 2012;47:6522.
- [35] Zhang C, Zhang F, Chen S, Cao W. *J Met* 2012;64(7):839.
- [36] <[http://en.wikipedia.org/wiki/Atomic\\_radii\\_of\\_the\\_elements\\_\(data\\_page\)](http://en.wikipedia.org/wiki/Atomic_radii_of_the_elements_(data_page))>; <<https://en.wikipedia.org/wiki/Electronegativity>>.